# Improvement of barrier properties of recycled thermoplastic polymers by $O_2$ and $NH_2$ functionalized graphene nanofillers

Dalal Alshammari[1*], Feras Korkees[2], Zeinhom M. El-Bahy[3], Yasmin Vieira[4,5], Guilherme Luiz Dotto[4*]

[1]Chemistry Department, College of Science, University of Hafr Al Batin, Hafr Al Batin, Saudi Arabia.

[2]Department of materials Science and Engineering, Swansea University, UK.

[3]Department of Chemistry, Faculty of Science, Al-Azhar University, Nasr City 11884, Cairo, Egypt.

[4]Research Group on Adsorptive and Catalytic Process Engineering (ENGEPAC), Federal University of Santa Maria, Av. Roraima, 1000, Santa Maria, RS, Brazil.

[5]Federal University of Pampa, Av. Pedro Anunciação, 111, 96570-000, Caçapava do Sul – RS, Brazil.

*Corresponding author: guilherme_dotto@yahoo.com.br; daalshammari@uhb.edu.sa

**Abstract**

Graphene/polymer composites have a wide range of applications, such as energy storage, 3D printing, sensors, water purification, and heat dissipation materials due to their enhanced mechanical, electrical, and thermal properties. One major challenge is graphene's tendency to aggregate due to strong Van der Waals interactions (5.9 kJ $mol^{-1}$), which hinders uniform dispersion in the polymer matrix. Therefore, this study focused on improving the barrier properties of recycled polymer matrices, such as Nylon 6, Nylon 66, and polyethylene terephthalate, against moisture using chemically modified graphene nanofillers (GNPs). The nanocomposite films were prepared based on the variation of GNPs' loadings and thicknesses. The results obtained from scanning electron microscope revealed that the addition of GNPs resulted in the formation of irregular protuberances on the fracture surface of the polymer matrices, with graphene fillers dispersed within the matrices. The water vapor transmission rate (WVTR) for samples with 0.5 mm was reduced by the addition of GNPs. The moisture barrier properties of recycled polymer matrices are improved by adding $O_2$- and $NH_2$- to GNPs, with interfacial interactions between the fillers and the matrices dependent on the functionalization type.

**Keywords**: absorption; barrier properties; graphene; nanocomposite; recycled polymers

## 1. Introduction

Human-designed composites have been significantly enhanced for use in various applications, from the sport and transportation sectors to military and aerospace engineering (Naskar et al. 2016). Among these, polymer-based nanocomposites incorporating nano-sized fillers of 0D, 1D, and 2D dimensions have garnered significant scientific interest (Lizundia et al. 2017; Moghadam et al. 2015). In this context, the inclusion of nanofillers was observed to enhance mechanical, thermal, electrical, and barrier properties, making these materials suitable for diverse applications. Several 2D materials, including $MoS_2$ and $WS_2$, have been tested for enhancing the conduction of these nanocomposites, but carbon-based materials such as graphene stand out due to their exceptional properties (Sun et al. 2021).

Graphene, in particular, has gained attention for its remarkable thermal conductivity and mechanical properties, which result from the strong interaction between polymer networks and the reinforcing phase (Yu et al. 2017). It exhibits the highest tensile strength values recorded for any material with an impressive specific surface area of 2360 $m^2\ g^{-1}$. Furthermore, it ranks among the best-known electrical conductors, with a conductivity of about $10^8$ S $m^{-1}$ (Zeinedini et al. 2018). Thus, graphene is considered an ideal nanofiller for polymer matrices (Yu et al., 2017), particularly due to its remarkable impermeability, making it an effective barrier material even against small diatomic gas molecules such as $He_2$ (Rajasekar et al., 2013). Damari et al. (2018), for example, found that a filler loading of 2% of graphene to polyurethane significantly improved water

barrier properties, which can be linked to the hydrophobic properties of the sp2 net in which graphene is organized.

Zahid et al. (2020) reported an 81% reduction in gas permeability in polyurethane films with 4% (wt.) multilayered graphene. Additionally, Kim and Macosko (2008) demonstrated that functionalized graphene reduced hydrogen permeability by 60% in poly(ethylene-2,6-naphthalate), compared to a 25% reduction with pristine graphene at the same filler loading. Even though these findings have shown the potential of graphene in polymeric applications, they also have shown that its performance depends on several factors, including its interaction with the polymer, defect density, lateral dimensions, and the number of layers (Ma et al. 2017). These challenges can be easily resolved when using pristine polymers, but still require more research when applied to recyclable polymers, which presents a promising opportunity for environmental sustainability and waste reduction (Tang and Chen 2019).

For example, Huang et al. (2014) developed a graphene oxide-regenerated cellulose nanocomposite that exhibited ultra-low oxygen permeability and excellent mechanical strength. Their study confirmed that by exfoliating and homogeneously dispersing graphene nanosheets, it could significantly enhance the recycled polymer's properties, achieving a 1000-fold reduction in oxygen permeability. Thus, these findings confirm that the overall characteristics of the resultant nanocomposites are largely influenced by graphene's distribution within the matrix, given its highly anisotropic nature (Wu et al. 2019). Still, most studies have focused on incorporating unmodified graphene into polymeric nanocomposites, which could result in limited effects (Sangroniz et al., 2019; Tseng et al., 2012; Méndez et al., 2017).

One major challenge is graphene's tendency to aggregate due to strong Van der Waals interactions (5.9 kJ $mol^{-1}$), which can hinder uniform dispersion in the polymer. To address this, graphene can be functionalized to improve compatibility with the polymer matrix (Korkees et al. 2021). Given these advancements, nanocomposites of recycled polymers, particularly those incorporating graphene-based nanofillers, hold tremendous potential for barrier applications. It can be concluded that the graphene/polymer composites are utilized in various applications, including energy storage, 3D printing, sensors, water purification, and thermal management, thanks to their superior mechanical, electrical, and thermal characteristics. A significant challenge arises from graphene's propensity to clump together due to strong van der Waals forces (5.9 kJ $mol^{-1}$), which complicates achieving a uniform dispersion within the polymer matrix. Thus, the effect of $O_2$- and $NH_2$-functionalized graphene nanofiller particles (GNPs) on the properties of recycled polymers such as Nylon 6 (PA6), Nylon 66 (PA66), and polyethylene terephthalate (PET) was studied. Incorporating recycled polymers like Nylon 6, Nylon 66, and PET as the matrix of the composites not only reduces costs but also enhances performance and sustainability. This approach aligns with modern environmental goals while delivering high-quality materials suitable for various applications. Furthermore, water permeability, water vapor transmission rate, water diffusion coefficient, and morphological behavior of the prepared composite materials were evaluated.

## 2. Methodology

### *2.1. Materials and sample preparation*

Perpetuus Carbon Technology supplied PA6, PA66, PET, and graphene ($O_2$–GNPs and $NH_2$–GNPs) for the study. Test samples were prepared using a high-temperature compression molding technique, with 12 samples produced for each thickness (0.09 mm and 0.5 mm) for PA6, PA66, and PET. The choice of thickness in the composite films is a critical factor that influences their properties and suitability for specific industrial applications. By selecting the appropriate thickness, manufacturers can optimize performance for the intended use, balancing flexibility, strength, conductivity, and cost-effectiveness. For example, 0.09 mm: Used in flexible electronics, sensors, and wearable devices. 0.5 mm: Suitable for intermediate applications, such as automotive parts, where moderate flexibility and strength are needed. PA6, PA66, and PET samples loaded with various ratios (0.5, 1, 2, and 5%) of $NH_2$ and $O_2$ functionalized graphene at 23°C. The PA6 films were prepared using a Moore Hydraulic press (Max 40 tons), while the PA66 and PET films were processed with a Fontijne press. Due to shear mixing, the temperature of the molten material increased beyond the set barrel temperature.

For PA6 film preparation, 25 g of pellets were heated to 260 °C with a temperature rate of 10 °C $min^{-1}$ with a dwell time of 7 min. A pressure of 8.5 MPa was applied by exerting 20 tonnes of force for 2 min, followed by cooling using a mold cooling system. PA66 films were prepared by heating 25 g of pellets at 265 °C for 2 min, after which a pressure of 7 MPa was applied using 16 tonnes of force for 2 min. The mold was subsequently cooled to room temperature with a cooling system, as illustrated

in Fig. S1 of the supplementary material. For PET films, the material was heated to 280 °C for 10 min and then compressed at a pressure of 18 MPa for an additional 10 min. The films were then quenched in an ice bath and dried in an oven at 40 °C for 24 h.

*2.2. Morphological analysis*

A field emission scanning electron microscope (FE-SEM, S-4800 Hitachi) with ultra-high resolution was utilized for analysis. The samples were initially exposed to liquid nitrogen (-196 °C) for 1–2 h before being freeze-fractured along a selected plane to examine the dispersion and interaction of nanofillers within the polymer matrix. The fractured samples were then affixed to the sample holder using silver paste and coated with a thin layer of platinum to prevent charging effects.

*2.3. Water vapor permeability and vapor transmission rates*

Water permeability was determined by the weight loss over a certain time using an aluminum cup, as shown in Fig. 1. The silicone sealant sealed the equalization valves, and a torque driver was employed to tighten the clamp bolts. The water vapor transmission rate (WVTR), which consists in measuring the amount of water vapor passing through a material over a specific period, was determined according to ASTM D6701 – 16 and calculated as read in Eq. (1), where: $G$ denotes the weight change (g), $t$ is the time (h) during which weight loss occurs, $A$ denotes the tested area of the sample ($m^2$), and $G/t$ is the weight loss per unit time (slope of the straight line). WVTR is measured in g $m^{-2}$ $h^{-1}$ (Randal Shogren, 1997).

$$WVTR = \frac{G/t}{A} \qquad \text{Eq. 1}$$

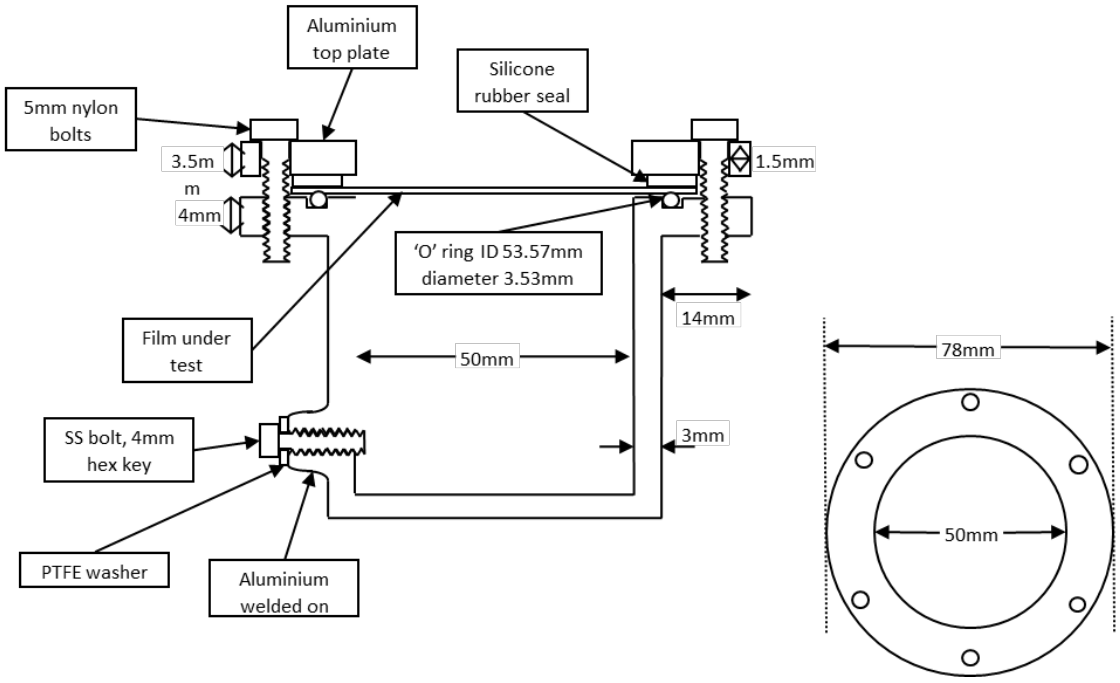


**Fig. 1.** Pot design for water vapor permeability test.

The samples were cut in a circular shape from the films, each bearing a diameter of 70 mm. Two unreinforced and GNP-reinforced samples of each thickness (0.09 and 0.5 mm) were tested in permeation. These sizes have been selected based on the most commonly used thickness in the packaging industry. Further, the samples were placed in a 155 mL distilled water aluminum cup covered with a gasket and clamped into a position.

*2.4. Water absorption*

A water absorption test was carried out on the two-thickness variant of the sample with the square dimensions of 2.5 cm×2.5 cm. The measurement was carried out on 1- and 2-mm-thick samples at 23, 40, and 70 °C. Sample variants were monitored until saturation through weight monitoring between 0.1mg (250g max) to 0.01mg (101g max).

The percentage of weight gain can be determined using Eq. 2 (Mahmoud et al., 2022), where $W_0$ denotes the actual dry weight, while $W_t$ represents the weight after immersion in water for a $t$ amount of time.

$$W\% = \frac{W_t - W_0}{W_0} \cdot 100 \qquad \text{Eq . 2}$$

*2.5. Statistical methodology*

All experiments were carried out in triplicate ($n$=3). For each triplicate of these experimental conditions, the standard error was estimated. Tukey's Honest Significant Difference (HSD) test was used to verify if there is a significant difference between the mean values at the 0.05 level (Agbangba et al., 2024).

## 3. Results and discussion

*3.1. Analysis of bonding and dispersion of GNPs in the polymer*

The SEM images of PA6, PA66, and PET are presented in Fig. 2a1–a4, 2b1–b4, and 2c1–c4, respectively. The analysis revealed that the freeze-fractured surfaces of pure PA6 and PA6/graphene composites, loaded with $O_2$- and $NH_2$-functionalized GNPs at concentrations of 1% and 5%, exhibited distinct features. The pure polymer matrices exhibit a relatively homogeneous structure, as seen in Fig. 2a1, 3b1, and 3c1. Upon the addition of 1% GNP, minor surface modifications are observed (Fig. 2a3, 2b3, and 2c3). As the filler concentration increases to 5%, the surface topography changes significantly, as illustrated in Fig. 2a2, 2b2, 2c2, 2a4, 2b4, and 2c4. The presence of graphene fillers induces the formation of irregular protuberances distributed across the fracture surface.

Regardless of the graphene content, the SEM images suggest that the fillers are relatively well dispersed within the polymer matrices, with no visible signs of debonding (Li et al., 2007). These findings align with our recent study on $O_2$- and $NH_2$-functionalized graphene-based recycled PA6 and PA66 composites (Korkees et al., 2021), as well as previous morphological analyses of graphene distribution in polymer matrices (Tseng et al., 2012).

Additionally, the SEM micrographs highlight differences in interfacial interactions between the graphene fillers and polymer matrices, as indicated by yellow arrows. Both functional groups successfully bonded with the polymer hosts; however, $NH_2$-functionalized graphene exhibited stronger adhesion compared to $O_2$-functionalized graphene. This finding is evident in the smoother, cleaner areas observed in the $O_2$-functionalized samples, suggesting weaker interfacial bonding. Nevertheless, both functional groups effectively disrupt the strong van der Waals forces between graphene particles, reducing aggregation (Korkees et al., 2021).

The SEM images of the lowest GNP loadings (Fig. 2a1, 2a3, 2b1, 2b3, 2c1, and 2c3) reveal that the exposed graphene fillers exhibit a relatively weakly wrinkled structure on the fractured surface. In contrast, at higher filler concentrations, the images show stronger interfacial interactions between the graphene and polymer matrix, as previously reported by Jeon et al. (Cho et al., 2017). This behavior may be attributed to the non-covalently functionalized amine groups on graphene, which facilitate hydrogen bonding with the carbonyl groups of the polymer chains, as also observed by Yang et al. (2012). Unlike pristine polymer matrices, the composites display crumpled and wrinkled graphene sheets. According to Mkhoyan et al. (2009), this surface topology results from

distortions in graphene sheets caused by residual oxygenated groups, structural defects, and their ultra-large aspect ratio. Moreover, the presence of large graphene flakes in the samples suggests that fillers with greater lateral dimensions are more likely to be confined within the polymer matrix and partially aligned within the film (Yousefi et al., 2013).

The SEM images further confirm the absence of significant agglomeration, indicating that the graphene nanofillers are well dispersed in the polymer matrix. Several factors may explain this dispersion. First, the wrinkled structure of the fillers suggests strong interfacial interactions, where oxygen-containing functional groups enable hydrogen bonding with the polymer's carbonyl groups. Second, large graphene flakes can become confined within the polymer matrix, increasing tortuosity. Moreover, the extrusion process may contribute to the alignment of graphene fillers within the polymer structure. Beyond SEM observations, another possible explanation for the improved dispersion is the increased penetration path created by impermeable graphene sheets, which may enhance the moisture barrier properties of polymer-graphene films. The synergistic combination of a high aspect ratio and well-aligned graphene sheets led to reduced mass loss in PET-$O_2$ (0.5 mm) and PET-$NH_2$ (0.09 mm) at 5 wt% graphene, with reductions of approximately 30 and 66%, respectively, compared to pristine polymers.

In conclusion, the interface interactions of functionalization species, specifically $O_2$ and $NH_2$, on the surface of graphene in composites with Nylon 6, Nylon 66, and PET play a crucial role in determining the barrier properties of these materials. The differences in functionalization can significantly influence the compatibility and bonding between graphene and the polymer matrix.

Oxygen-containing groups (e.g., hydroxyl, carboxyl) onto the graphene surface enhance the hydrophilicity of graphene, which can improve its dispersion in polar polymer matrices like Nylon 6 and Nylon 66 through strong hydrogen bonding interactions with the amide groups (Fig.2) (Mahmoud et al., 2023).

On the other hand, $NH_2$ functionalization increases the reactivity of graphene and can enhance its compatibility with both Nylon and PET. The amino groups can form covalent bonds with the carbonyl groups present in Nylon and PET, leading to improved interfacial strength and better load transfer between the graphene and the polymer matrix. $NH_2$ functionalization generally provides stronger covalent bonding compared to $O_2$ functionalization, which primarily relies on non-covalent interactions (e.g., hydrogen bonding). This behavior can lead to better mechanical performance in composites, particularly in Nylon 6 and Nylon 66, which have strong polar interactions (Korkees et al., 2021). In contrast, while $O_2$ functionalization can enhance dispersion, it may not provide the same level of mechanical reinforcement as $NH_2$ functionalization due to weaker bonding mechanisms. Therefore, the results show that composites with $NH_2$-functionalized graphene exhibit lower water vapor transmission rates (WVTR) compared to those with $O_2$-functionalized graphene. This is attributed to the stronger interfacial interactions that reduce the pathways available for moisture diffusion.

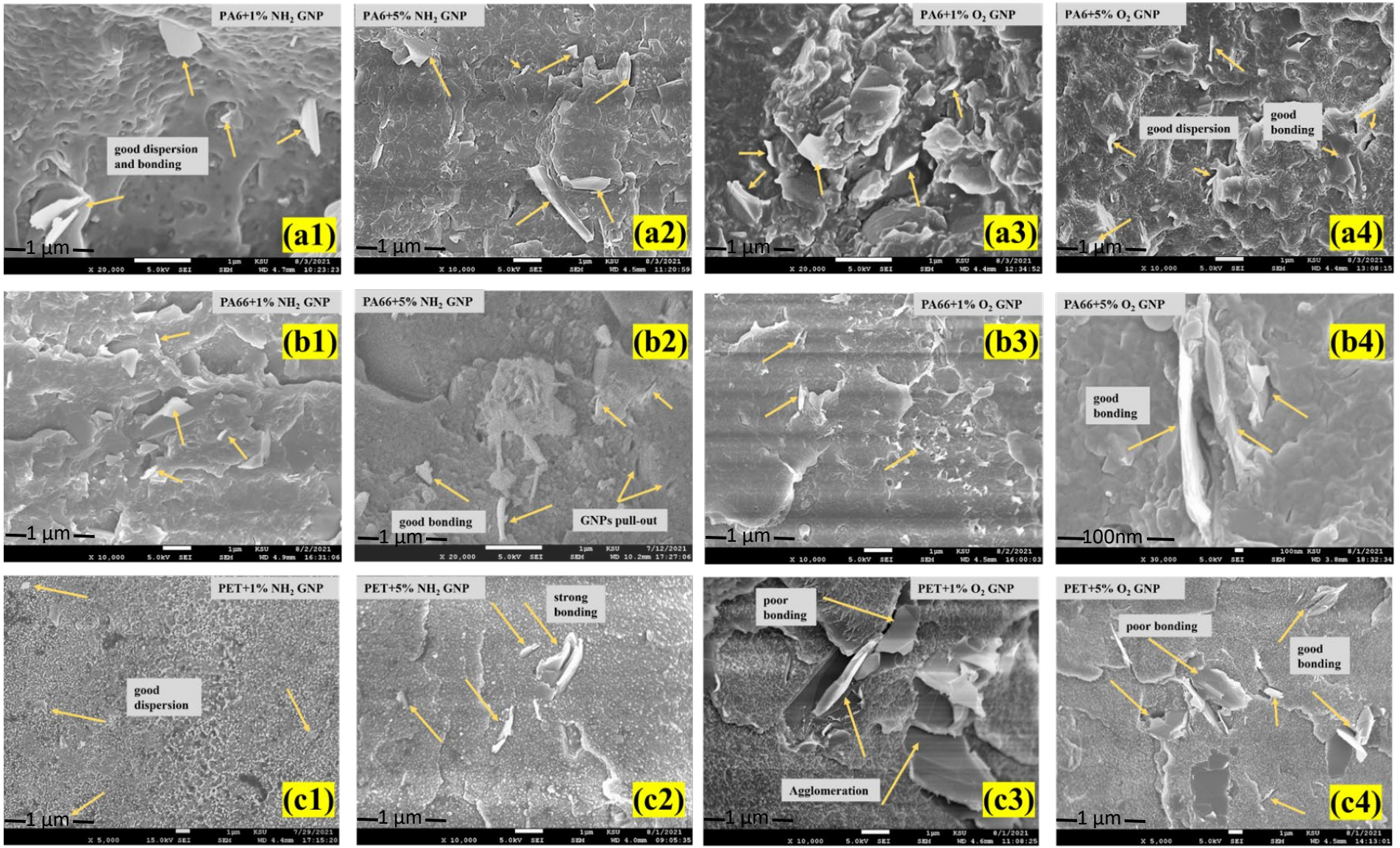


**Fig. 2.** SEM micrographs of freeze-fractured surfaces of PA6, PA66, and PET composites with 1 and 5 wt% graphene nanoplatelets (GNPs) functionalized with $NH_2$ and $O_2$, where: (a1) PA6 with $NH_2$-functionalized GNPs at 1 wt%; (a2) PA6 with $NH_2$-functionalized GNPs at 5 wt%; (a3) PA6 with $O_2$-functionalized GNPs at 1 wt%; (a4) PA6 with $O_2$-functionalized GNPs at 5 wt%; (b1) PA66 with $NH_2$-functionalized GNPs at 1 wt%; (b2) PA66 with $NH_2$-functionalized GNPs at 5 wt%; (b3) PA66 with $O_2$-functionalized GNPs at 1 wt%; (b4) PA66 with $O_2$-functionalized GNPs at 5 wt%; (c1) PET with $NH_2$-functionalized GNPs at 1 wt%; (c2) PET with $NH_2$-functionalized GNPs at 5 wt%; (c3) PET with $O_2$-functionalized GNPs at 1 wt%; (c4) PET with $O_2$-functionalized GNPs at 5 wt%.

*3.2. Water vapor permeability and transmission rate*

Figure 3a-f shows the weight change over time for recycled PA6, PA66, and PET samples loaded with $NH_2$ (left) and $O_2$ (right) functionalized graphene at varying concentrations. The mass loss of all samples displayed an approximately linear relationship with exposure time, indicating homogeneous moisture transmission (Yousefi et al., 2013). For PA6 samples (Fig. 3a and 3b), a sharp decline in weight was observed, with nearly all variants exhibiting mass losses between 1000 and 2000 mg. Interestingly, pristine PA6 experienced the least weight loss, whereas the samples loaded with 5% $O_2$- and $NH_2$-functionalized graphene showed the highest values, exceeding 1500 mg and 2000 mg, respectively, over 1200 hours.

For PA66 samples (Fig. 3c and 3d), the mass loss was even more pronounced, reaching up to 3500 mg for 5% $NH_2$ loading and approximately 2200 mg for 5% $O_2$ loading. Notably, the 1% $O_2$-loaded PA66 exhibited the lowest mass loss. A trend similar to PA6-$NH_2$ was observed in PA66-$NH_2$, where pristine PA66 showed lower weight loss. However, in PA66-$O_2$ samples, the presence of graphene nanoplatelets (GNPs) reduced mass loss compared to pristine PA66, demonstrating a contrasting trend.

For PET samples, mass loss was significantly lower than in PA6 and PA66. Pristine PET exhibited the least weight reduction compared to the PET-$NH_2$ variants. The 2 and 5% PET-$NH_2$ samples showed lower mass loss than the 0.5 and 1% PET-$NH_2$ variants. Conversely, 1% PET-$O_2$ displayed a rapid and substantial mass loss, reaching approximately 900 mg over 1200 h. However, PET samples with 0.5, 1, and 2% $O_2$ functionalization followed a similar weight loss trend. The influence of $NH_2$- and $O_2$-functionalized graphene on PET at 2 and 5% concentrations was more pronounced

compared to PA6 and PA66, where only $O_2$-functionalized graphene significantly reduced PA66 mass loss.

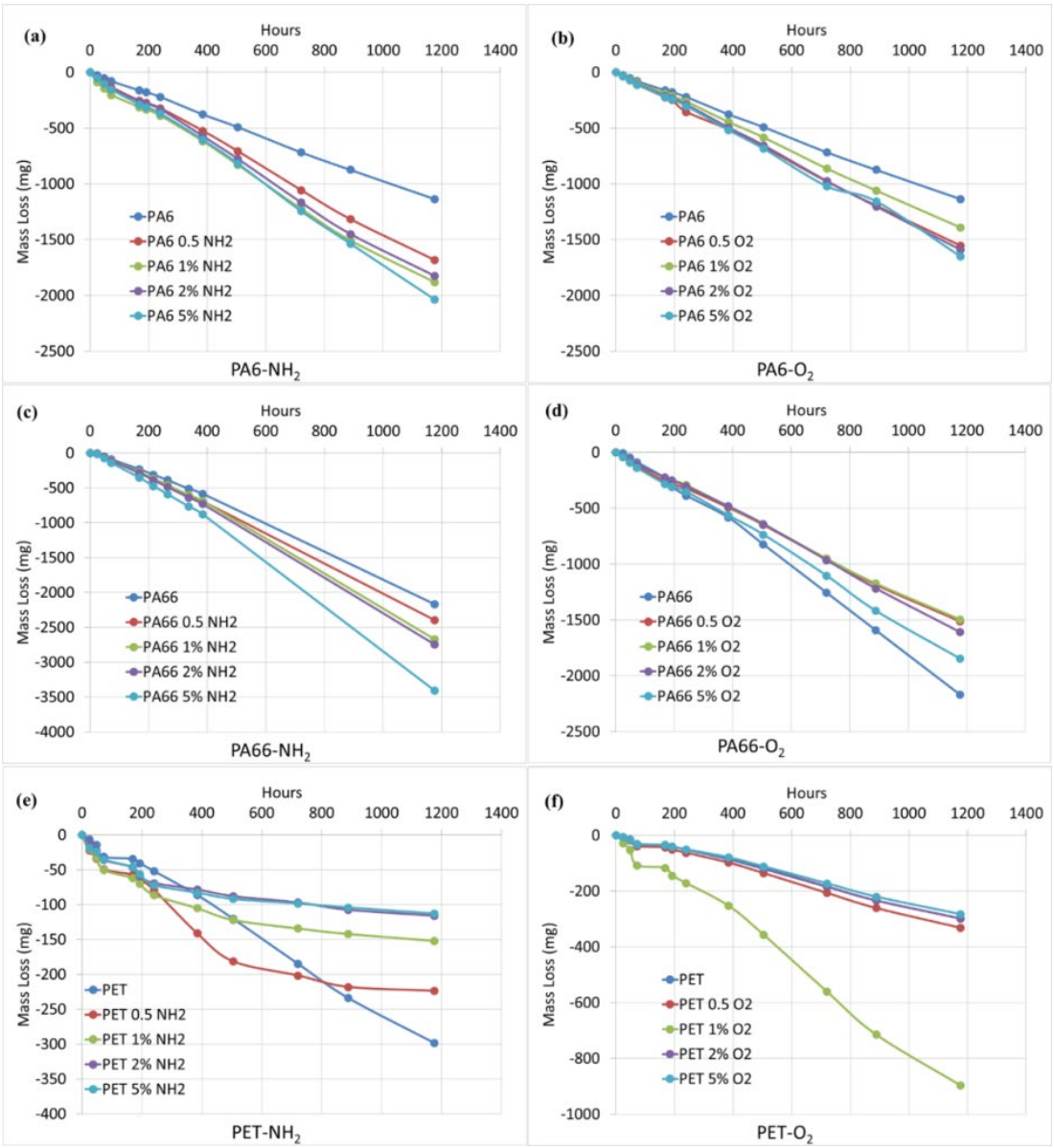


**Fig. 3:** Mass loss in mg with time for the (left) $NH_2$ and (right) $O_2$ functionalized graphene loaded (a, b) PA6, (c, d) PA66, and (e, f) PET samples of thickness 0.09mm. (Each experimental point is a mean of three equal experiments ($n$=3). The maximum standard error was 2.02%).

The 5% $NH_2$-PET sample exhibited the lowest mass loss, around 100 mg (Fig. 3e), with the 5% $O_2$-PET sample showing similarly minimal loss (Fig. 3f). This suggests

a significant barrier effect provided by the functionalized graphene nanoparticles, likely due to enhanced interactions between the polymer matrix and the graphene additives, reducing water permeability. In contrast, the 1% $O_2$-PET sample exhibited a drastic mass reduction, reaching nearly 900 mg over 1200 hours. This behavior may be attributed to insufficient dispersion or aggregation of graphene nanoparticles at lower loadings, leading to inconsistencies in the polymer network and increased moisture transmission pathways.

These results reinforce the hypothesis that graphene nanoparticle incorporation decreases polymer permeability by altering the polymer's microstructure and crystallinity. The enhanced barrier properties observed in higher-loading samples, particularly at 5%, indicate a threshold concentration above which functionalized graphene contributes significantly to moisture resistance. Li et al. (2019) reported that adding $O_2$-GNPs to polymer blends slightly increased the crystallinity of both PA6 and PA66 at 0.1% content, followed by a gradual decrease as the GNP content increased. This trend suggests that while low concentrations of $O_2$-GNPs may act as nucleating agents, enhancing crystallinity, excessive GNPs disrupt polymer chain alignment, reducing overall crystallinity and, consequently, affecting moisture barrier properties.

The permeability values for mass loss over 1200 h for the 0.5 mm thick samples are shown in Fig. 4, which achieved lower permeability while increasing the functionalized loading content in the polymer matrices. Surprisingly, all the 0.5 mm thick samples depicted the lowest permeability (least mass loss) at 5% of the $NH_2$ and $O_2$ functionalization loading. As this trend was not observed in thinner samples, the permeability behavior may be thickness-dependent. The optimization of filler content

was therefore necessary to determine the most appropriate concentration for each sample type. Nevertheless, for the 0.5 mm thick samples, the 5% filler loading consistently proved to be the optimum concentration.

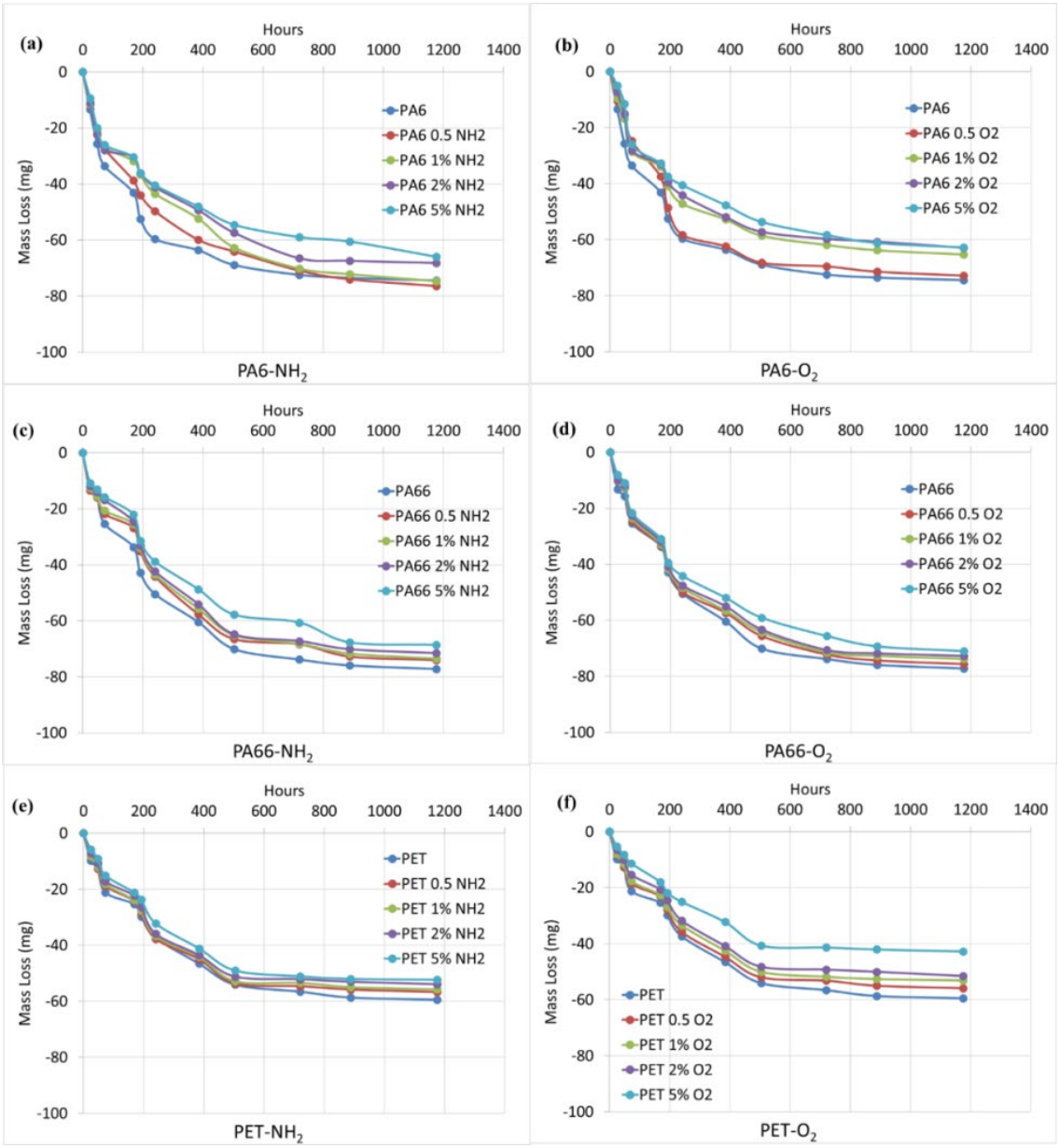


**Figure 4:** Graphical illustration of mass loss in mg with time for the (left) $NH_2$ and (right) $O_2$ functionalized graphene loaded (a, b) PA6, (c, d) PA66, and (e, f) PET samples. The thickness of the samples was set to be 0.5 mm. (Each experimental point is a mean of three equal experiments ($n$=3). The maximum standard error was 1.25%).

The observed variations in mass loss with thickness highlight the interplay between polymer microstructure and graphene nanoparticle dispersion. The initial sharp decrease in mass content is likely due to surface water evaporation, followed by steady mass loss over time. The incorporation of $O_2$ and $NH_2$ functionalized GNPs in PA6, PA66, and PET reduced mass loss by introducing a tortuous path that restricts moisture diffusion, while also improving the mechanical, tensile, and thermal properties of the polymer (Xu et al. 2015). This thickness-dependent permeability behavior aligns with prior findings that some polymers serve as excellent gas barriers when dry but perform poorly under humid conditions due to the disruptive effect of hydrogen bonds (H-bonds) binding the polymer matrix (Feron et al. 1994). Polymers with high polarity, particularly those containing hydroxyl groups, effectively block gas permeability but exhibit lower resistance to water vapor transmission. Thus, the optimization of graphene nanoparticle content concerning polymer thickness plays a crucial role in enhancing both moisture and gas barrier properties. Additionally, plasticization by water induces poor gas barrier properties in them. Conversely, due to their high non-polarity, hydrocarbon polymers exhibit excellent water barrier characteristics but poor gas barrier characteristics (Salame and Steingiser 1977).

Unlike traditional composites, polymer nanocomposites (PNCs) incorporate fillers with dimensions below 100 nm. Since their initial development by the Toyota Group (Okada et al., 1990), extensive research has been conducted in this field. The significance of PNC technology extends beyond merely improving the mechanical properties of the base polymer or substituting less effective fillers. Rather, their importance is acknowledged because these composites add value to the properties of the pristine

polymers without compromising the inherent mechanical properties, and they possess easy processability and lightweight (Verdejo et al. 2011). Hence, the barrier properties can be improved without compromising the resin's inherent processability or adding extra weight. Notably, the size and characteristics of nanofillers are critical in the design and behavior of the PNCs, as well as the interface between the matrix and the nanofillers (Terrones et al. 2011). Moreover, the content of filler particles in these composites is < 5 wt.%, and they ultimately induce a significant reduction in the gas and water permeability, as well as enable the retention of the inherent processability and toughness of the pristine polymer (Tan and Thomas 2016). Table 1 summarizes the lowest and highest mass loss values for both thicknesses.

**Table 1.** Lowest and highest mass loss (mg) values as a function of time for 0.09 and 0.5 mm thick PA6, PA66, and PET samples loaded with 0.5, 1, 2, and 5% $NH_2$ and $O_2$ functionalized graphene at 23°C.

| **Functionalization** | **Mass loss values** | **Samples with (%) $O_2$ and $NH_2$ loadings** | | | | | |
|---|---|---|---|---|---|---|---|
| | | **PA6** | | **PA66** | | **PET** | |
| | | **0.09mm** | **0.5 mm** | **0.09mm** | **0.5 mm** | **0.09mm** | **0.5mm** |
| **$NH_2$** | Lowest | Pristine | Pristine | Pristine | Pristine | 5 % $NH_2$ | Pristine |
| | Highest | 5 % $NH_2$ | 5%$NH_2$ | 5 % $NH_2$ | 5 % $NH_2$ | Pristine | 5 % $NH_2$ |
| **$O_2$** | Highest | Pristine | Pristine | 1 % $O_2$ | Pristine | 5 % $O_2$ | Pristine |
| | Lowest | 5 % $O_2$ | 5 % $O_2$ | Pristine | 5 % $O_2$ | 1 % $O_2$ | 5 % $O_2$ |

Most importantly, a significant difference between the mass loss values depicted in Fig. 3 and 4, corresponding to 0.09 mm and 0.5 mm thickness, respectively, proves the pronounced effect of thickness on the mass loss properties of the polymeric systems. It is widely accepted that permeability largely relies on temperature and pressure, as in this study. However, as reported by Hwang Kammermeyer (1974) and observed in this study, the thickness can be a critical parameter in determining the permeability values. For all polymeric systems investigated during this study, it is evident that the mass loss for the

0.5 mm samples is several orders of magnitude less than that for the 0.09 mm samples. Also, the mass loss values depend on the type of functionalization. In this context, composites with $O_2$ functionalized graphene exhibit relatively lower mass loss compared to $NH_2$ functionalized polymeric systems. This behavior holds for all three recycled polymeric systems employed in this study. However, this difference is insignificant for the thicker samples (0.5 mm), and the values for both types of functionalization do not vary much. Thicker samples might also mean that less agglomeration of GNPs might occur, and better dispersion might be obtained, creating more complex paths for water molecules. Carbonaceous materials, i.e., carbon nanotubes or carbon black and layered silicates-based PNCs, have been widely explored owing to their mechanical and electrical characteristics and good barrier properties (Huang 2022). Graphene has led to the rise of a new class of PNCs. It has been widely reported that materials with a high aspect ratio increase the tortuosity of the path. As permeability depends on the diffusion of gas and solubility, a tortuous and complex path obtained on the dispersion of high aspect ratio materials inside a polymer matrix increases the barrier properties (Huang 2002).

### *3.3. Water vapor transmission rate (WVTR)*

The water vapor transmission rate (WVTR), also called moisture vapor transmission rate, is the measure of water passage through an area of a substance in a specified time, temperature, and humidity conditions (Keller and Kouzes 2017). It is measured in mass per area per time. The measurement is valid for all sorts of vapor (Bell and Labuza 2000). Generally, it is related to the water/moisture barrier applications.

The values of WVTR for the unfilled PA6, PA66, and PET films and the same films reinforced with 0.5, 1,2, and 5% loading of $O_2$ and $NH_2$ functionalized graphene were calculated and tabulated in Table 2. Figure 5a illustrates the WVTR of $O_2$ and $NH_2$ functionalized graphene-reinforced PA6 films compared to the unfilled PA6 films. The WVTR for $NH_2$-PA6 and $O_2$-PA6 decreased with increasing GNPs content, with a 17% drop at 5%. However, 0.09 mm showed a significant increase (50%) in WVTR, going from 0% to 0.5% GNPs, then that followed but not much different, and fluctuation with increasing GNPs content. The highest values for the $O_2$ and $NH_2$ variants are determined to be $385.08\times10^{-7}$ (mg $mm^{-2}$ $h^{-1}$) $mm^{-1}$ at 2% loading and $491.43\times10^{-7}$ (mg $mm^{-2}$ $h^{-1}$) $mm^{-1}$ at 5% loading, respectively. In comparison, the lowest values were recorded at 1 and 0.5 % loading for $O_2$ and $NH_2$ variants and determined to be 339.28 and $421.20\times10^{-7}$ (mg $mm^{-2}$ $h^{-1}$) $mm^{-1}$, respectively. Table 2 presents values for all three polymeric systems.

**Table 2.** Water transmission rate ($10^{-7}$ (mg $mm^{-2}$ $h^{-1}$) $mm^{-1}$) of 0.09- and 0.5-mm PA6, PA66, and PET variants at different $O_2$ and $NH_2$ loadings.

| | | **Water transmission rate ($10^{-7}$ (mg $mm^{-2}$ $h^{-1}$) $mm^{-1}$)** | | | | | |
|---|---|---|---|---|---|---|---|
| | | **PA6** | | **PA66** | | **PET** | |
| **Loadings (%)** | **Functionalization** | **0.09 mm** | **0.5 mm** | **0.09 mm** | **0.5 mm** | **0.09 mm** | **0.5 mm** |
| 0.00 | - | 279.51 | 130.75 | 509.63 | 135.01 | 74.83 | 104.24 |
| 0.5 | $NH_2$ | 421.20 | 131.64 | 558.98 | 129.32 | 112.53 | 99.26 |
| 1 | $NH_2$ | 482.39 | 128.43 | 614.00 | 127.54 | 73.28 | 97.66 |
| 2 | $NH_2$ | 463.86 | 119.89 | 632.82 | 124.70 | 55.41 | 94.28 |
| 5 | $NH_2$ | 491.43 | 107.62 | 783.01 | 120.43 | 53.76 | 92.50 |
| 0.5 | $O_2$ | 382.31 | 127.01 | 379.04 | 132.17 | 83.38 | 97.66 |
| 1 | $O_2$ | 339.28 | 113.31 | 375.38 | 129.32 | 228.59 | 93.57 |
| 2 | $O_2$ | 385.08 | 107.98 | 389.69 | 127.72 | 74.67 | 88.94 |
| 5 | $O_2$ | 370.13 | 108.69 | 453.63 | 123.10 | 70.44 | 74.71 |

Figure 5b presents WVTR for PA66 polymer-functionalized ($O_2$ and $NH_2$) graphene nanocomposite at different filler concentrations compared to the unfilled PA66 films. Similar to the PA6 sample, the 0.5 mm sample showed an almost 11% reduction in

WVTR for both types of GNPs, which is an improvement due to the presence of GNPs. However, the 0.09 mm samples showed a significant reduction in WVTR for $NH_2$ by 28.6% for the 5% filler loadings. While for $O_2$, WVTR declined by 17.2%. Further, the PET showed a trend similar to that of PA6 and PA66, with only a small variation, as shown in Figure 5c, for 0.5 mm samples. However, the variations are noticeable in the case of the $O_2$ variant of 0.5 mm PET samples; WVTR dropped by 23.4%. In the case of 0.09 mm samples, it declined by 52.2% for $NH_2$ and 69.1% for $O_2$. This significant drop is considered a great success for the application.

Water permeability is a complex process influenced by the high polarity of water molecules, which enables strong interactions with specific polymers and facilitates hydrogen bonding. These interactions can lead to swelling and increased chain mobility within the polymer structure. The permeability characteristics of water differ depending on its physical state due to variations in molecular kinetic energy. In its vapor state, water molecules are in constant motion, with an average velocity of approximately 450 m $s^{-1}$, whereas liquid water has significantly lower kinetic energy. Additionally, capillary effects may contribute to differences in permeability, where liquid water movement is restricted while vapor transmission remains largely unaffected (Sangaj and Malshe, 2004). Permeation is a rate-driven process primarily governed by temperature and concentration gradients, which influence the diffusion of molecules across a medium. Hydrophilic polymers tend to facilitate water diffusion as concentration increases, with permeability being highly dependent on absolute vapor pressure due to the corresponding rise in solubility. Conversely, hydrophobic polymers may exhibit reduced diffusivity at higher concentrations, as water molecules tend to cluster. As a result, water transport

through polymer films is influenced by multiple factors, including pressure variations across the material, water solubility within the polymer, film thickness, and its overall physical condition (Guan, 2017).

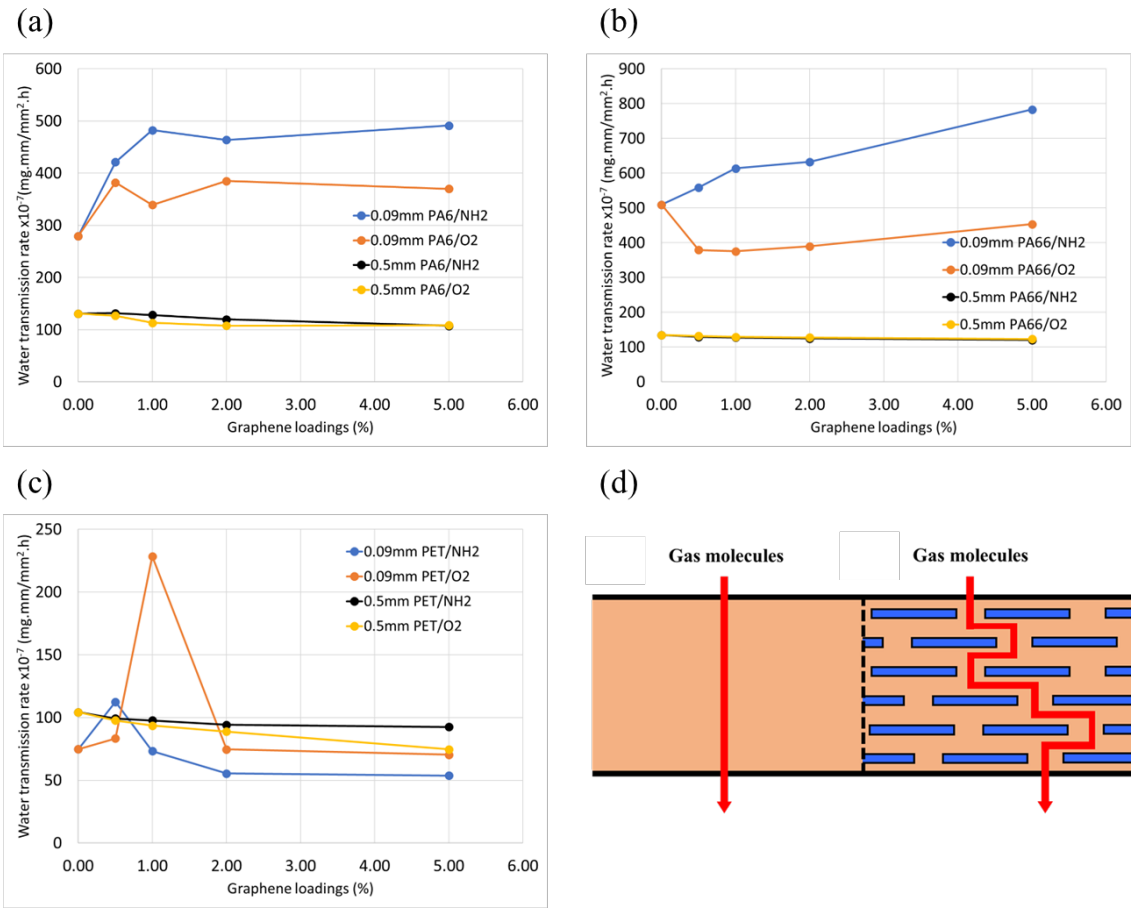


**Fig. 5.** (a) Water vapour transmission rate as a function of 0.5,1,2 and 5 % $NH_2$ and $O_2$ functionalized graphene loading in PA6. (b) Water vapour transmission rate as a function of 0.5, 1, 2, and 5% $NH_2$ and $O_2$ functionalized graphene loading in PA66. (c) Water vapour transmission rate as a function of 0.5, 1, 2, and 5% $NH_2$ and $O_2$ functionalized graphene loading in PET. (d) Schemes representing the straight path and tortuous path of the nanocomposites due to the presence of GNP. (Each experimental point is a mean of three equal experiments ($n$=3). The maximum standard error was 3.37%).

Figures 5a-5c graphically describe the permeability evaluation of the polymer composite films loaded with $O_2$ and $NH_2$ functionalized graphene. It is shown that the

mass loss has improved significantly by adding graphene with functionalized groups for PA66-5%-$O_2$ by about 18% and PET-5%-$NH_2$ by about 63% compared with unmodified composite materials with a thickness of 0.09mm. In the samples with 0.5mm, the mass loss has improved for PA6PA6-5%-$NH_2$ by about 13%, PA5-5%-$O_2$ by about 17%, PA66-5%-$NH_2$ by about 10%, PA66-5%-$O_2$ by about 8%, PET-5%-$NH_2$ by about 8%, and PET-5%-$O_2$ by about 30% in comparison with unmodified samples. The results indicated that the $NH_2$ functionalized graphene significantly reduces the mass loss for PET at a thinner thickness (0.09mm). In comparison, all thicker samples (0.5mm) showed a slight improvement by adding 5 wt% of functionalized graphene.

As discussed above, the 0.09 mm thick samples show a linear trend in the mass loss curve as a function of time. It is reported that such a phenomenon indicates the homogeneous dispersion of nanofillers into the polymer matrix (Yousefi et al. 2013). However, the thicker samples (0.5 mm) of the same variants showed remarkable improvement in the water permeability, and mass loss was significantly reduced (Figure 5d). Table 2 clearly shows that a 5% filler loading of both $O_2$ and $NH_2$ functionalized graphene gave the best performance, which is attributed to the presence of graphene in the polymer matrix and can be explained by several reasons. Firstly, our study revealed that WVTR for PA66 polymer-functionalized ($O_2$ and $NH_2$) graphene nanocomposite at different filler concentrations in comparison to the unfilled PA66 films.

Similar to the PA6 sample, the 0.5 mm sample showed an almost 11% reduction in WVTR for both types of GNPs, which is an improvement due to the presence of GNPs. However, the 0.09 mm samples showed a significant reduction in WVTR for $NH_2$ by 28.6% for the 5% filler loadings. While for $O_2$, WVTR declined by 17.2%. Further,

the PET showed a similar trend to PA6 and PA66 for 0.5 mm samples. However, the variations are noticeable in the case of the $O_2$ variant of 0.5 mm PET samples; WVTR dropped by 23.4%. In the case of 0.09 mm samples, it declined by 52.2% for $NH_2$ and 69.1% for $O_2$. This significant drop is considered a great success for the application.

It has already been reported that graphene fillers over 2 wt.% show a significant orientation of graphene sheets because they tend to self-adjust their basal plane perpendicular to the thickness of the film, which results in the partial alignment of the graphene layers. It is also noteworthy that graphene sheets are better aligned if their content in the composite is increased (Korkees et al. 2021). The well-aligned graphene sheets were observed at higher wt.% content (5%) with protruding ridges ascribed to the parallel running sheets of graphene (Yousefi et al. 2013). Hence, as per the hypothesis of this work, the alignment of graphene sheets increases when the graphene content is increased. This self-orientation of graphene-based fillers has been widely reported, and it also holds for clay and carbon nanotubes (Ma et al. 2010).

In the context of graphene, Ansari et al. prepared highly self-aligned graphite nanosheets with good dispersion in the polymer matrix without needing any external force (Ansari et al. 2010). Similarly, Yousefi et al. reported a polymer-graphene composite with fine dispersion and well-aligned graphene sheets, another example indicating self-aligned graphene (Yousefi et al. 2012). It is highly desired to produce homogeneous graphene with profound interfacial interaction in the polymer-graphene composites. This trend was expected in our case due to carboxyl chains in the polymer chains and the oxygenated group in the graphene. Particularly, nanofillers have to be functionalized to achieve good dispersion and interfacial interaction with the polymer

matrix, which was achieved during this work. It is important to note that well-dispersed nanoparticles in the polymer matrix and their strong bonding with the host matrix can lead to almost no aggregation and, ultimately, excellent dispersion that can be achieved through functionalization.

The functionalized graphene can break strong van der Waals forces between carbon nanoparticles, responsible for agglomeration. Conversely, the diffusion mechanism of water vapor in graphene/polymer composites encompasses several important concepts, including the creation of a "tortuous path." This phenomenon can greatly influence water vapor permeability and is shaped by both theoretical models and experimental findings (Fig. 5). A tortuous path describes a complex route that the diffusing molecules must navigate through the material. In graphene composites, the nanoparticles form an intricate network that modifies the directness of the diffusion pathway. When graphene is incorporated into the polymer matrix, it establishes a network that can obstruct or redirect the linear paths available for water vapor diffusion. This structure extends the effective distance water vapor must travel, thereby increasing resistance to permeation. SEM analysis results illustrate the distribution and arrangement of graphene within the polymer matrix, shedding light on how these structures contribute to tortuosity (Fig. 2).

The well-aligned and dispersed GNPs can improve the permeation rate, but increasing the GNPs' content means that it also becomes possible due to the 'tortuous path' provided by the percolating network of platelets, which prevents the diffusion of molecules through the matrix. Thus, permeability can be significantly reduced (Figure 5d). Also, the strong dispersion and interfacial bonding between the host polymer matrix

and the functionalized graphene fillers lead to better mechanical and thermal properties (Liu et al. 2010). The type of functionalization also plays a critical role in our results.

Similar to the PA6 sample, the 0.5 mm sample exhibited an approximately 11% decrease in WVTR for both $NH_2$- and $O_2$-functionalized graphene nanoparticle (GNP) loadings, demonstrating the effectiveness of GNP incorporation in enhancing barrier properties. In contrast, the 0.09 mm samples showed a more pronounced reduction, particularly for $NH_2$-functionalized graphene, which led to a 28.6% decrease at a 5% filler loading, while the $O_2$-functionalized variant reduced WVTR by 17.2%.

PET followed a similar trend to PA6 and PA66 in the 0.5 mm samples, with only minor deviations (Figure 5a). However, significant differences were observed in the 0.5 mm PET samples modified with $O_2$-functionalized GNPs, where WVTR declined by 23.4%. The effect was even more pronounced in the 0.09 mm PET samples, which exhibited a WVTR reduction of 52.2% for $NH_2$-functionalized graphene and 69.1% for $O_2$-functionalized graphene. This substantial decrease highlights the success of these modifications in improving moisture resistance.

The strong interfacial interactions between the amine groups on graphene and the N-H groups in nylon contribute to improved chemical compatibility, as observed when $NH_2$-functionalized graphene was used (Korkees et al., 2021). Gojny et al. (2005) found that amino-functionalized carbon-based materials enhance polymer nanocomposite properties by improving dispersion stability due to their strong interactions with the polymer matrix. This behavior is attributed to the increased polarity of functionalized carbon materials and the potential for covalent bonding between amino groups and the polymer structure (Keledi et al., 2012). The ability of $NH_2$-functionalized graphene to

form covalent bonds with the polymer matrix strengthens interfacial adhesion, further improving the overall performance of PET-based nanocomposites.

According to the above discussion, it can be concuded that the differences in water vapor WVTR observed in the composites, particularly between thin (0.09 mm) and thick (0.5 mm) samples, can be refered to various mechanisms such as: (1) Morphological Differences: Thinner films may show a more uniform distribution of graphene, resulting in a more continuous pathway for water vapor diffusion. The decreased thickness can also reduce the number of defects, improving barrier properties. Thicker samples might exhibit greater agglomeration of graphene, leading to irregularities and voids that can increase the WVTR. (2) Diffusion Pathway: In thinner films, water vapor has a shorter distance to travel, which may lead to reduced resistance to permeation. The routes for vapor transport are more straightforward and less hindered by the material matrix. In contrast, thicker films can lengthen the diffusion pathway, potentially increasing the overall resistance to water vapor movement, while also providing more chances for moisture to become trapped or to discover alternative routes. (3) Interfacial Interactions: The level of interaction between graphene and the polymer matrix can change depending on the thickness. Thinner films may facilitate better interfacial adhesion, which can enhance barrier properties, whereas thicker films may demonstrate weaker interactions that influence water vapor transmission rate (WVTR). In this study, since the graphene is functionalized, the impact of these functional groups may be more significant in thinner films, thereby improving water vapor resistance. (4) Hydrophilicity and Hydrophobicity: Water vapor permeability can differ greatly depending on the intrinsic properties of the polymer, and this effect may vary between

thin and thick films. Additionally, incorporating graphene modifies the overall hydrophilicity of the composite. In thinner films, graphene can notably improve barrier properties by obstructing water vapor diffusion.

The variations in WVTR for modified graphene/Nylon 6, Nylon 66, and PET composites in thin versus thick samples are affected by factors such as morphological features, diffusion pathways, interfacial interactions, and hydrophilicity. Grasping these mechanisms is essential for optimizing the design of composites for particular applications, especially in environments sensitive to moisture.

*3.4. Water absorption analysis and determination of diffusion coefficients*

The primary goal of absorption experiments was to investigate the effect of functionalized GNPs on the absorption behavior of these recycled polymers. It was hoped that adding GNPs would improve their resistance to moisture absorption. Nylon contains hydrophilic amide groups. Therefore, nylon is a water-absorbent that absorbs moisture from the surrounding environment at high levels. Therefore, it was hoped that adding GNPs would increase their resistance to moisture absorption, which can make a new market for them. Thus, widen their applications. It was also aimed to analyze the change in the diffusion coefficients of the materials under test when they were subjected to moisture over time. The key parameters influencing water absorption include time, relative humidity, and temperature.

The samples' thickness variants (1 and 2 mm) were tested at 23, 40, and 70 °C against time for PA6, PA66, and PET samples loaded with 0.5, 1, 2, and 5% of $NH_2$ and $O_2$ functionalized graphene. Water uptake was evaluated by measuring the percentage

increase in weight over time. The data were plotted as absorption (%) against the square root of time to analyze the samples' absorption behavior. Figure 6a shows the samples exposed to water at 23 °C, while Figures 6b and 6c show equivalent results at 40 and 70 °C, respectively. The PA6 samples (1 mm) loaded with 5% $O_2$ functionalized GNPs showed the least weight gain (~ 7%), while PA6 1% $NH_2$ showed the highest weight gain (11%). Similarly, the 2 mm thick PA6 sample showed the same trend for the lowest weight gain, while 2% $O_2$ showed the highest content. Consequently, PA6 samples loaded with 5% $O_2$ GNPs exhibited the least weight gain (7%) in both thickness variants of the samples. For PA6 samples, a sharp decline in the weight has been observed, and almost all variants of samples exhibited a mass loss between 1000 and 2000 mg in our study, as shown in Figures 5a and 5b.

The water uptake trend for 1 and 2-mm-thick recycled PA66 samples. The lowest absorption was recorded for 5% $O_2$ (7%) and 0.5% $O_2$ (5.5%), while the highest values were recorded for 5% $NH_2$ (10%) and 1% $NH_2$ (6%) samples, respectively. However, recycled PET samples showed a remarkable reduction in water gain, and a maximum of up to 1.4 % absorption was recorded for both thickness variants. The lowest values were recorded for 1 % $NH_2$ and 5 % $O_2$ (0.8 and 0.6 %) samples, while the highest values (1.4%) were recorded for 1% $O_2$ and 0.5% $NH_2$ samples for 1 and 2mm thicknesses, respectively. In summary, the PET composite with O2 and NH2 functionalized graphene proved to be the most resistive material to moisture absorption, exhibiting remarkably lower values —typically below 1.5% water gain — compared with PA6 and PA66, which showed a water content increase between 4% and 11.5%. In conclusion, recycled PET demonstrated the highest durability, as it exhibited a lower tendency to absorb water at

room temperature. Notably, moisture uptake occurs rapidly during the initial absorption phase. Subsequently, water absorption shows an approximately linear relationship with the square root of exposure time, followed by a slower increase until saturation is reached.

In the case of recycled PA6 (Figures 6b and 6c) at 23 °C, the curves showed a sharp increase in the water uptake in the initial stage, with increased water uptake at 8% and 8.5% in 225 and 625 hours. However, it almost showed a straight line (saturated) after the time above, with no further significant gain in weight. The thickness of the samples was determined to be 0.09 mm. The mass loss of all the samples depicted a linear relationship versus exposure time, indicating homogeneous moisture transmission. The diffusion in simple gases such as $O_2$, $H_2$, and $CO_2$, in addition to water and liquids, is dominated by the random steps between the polymer chains and exhibits ideal Fickian behavior.

According to Henry's law, the diffusion coefficient "D" remains constant regardless of time and concentration. However, the diffusion of water vapors through hydrophobic polymers generally manifests ideal diffusion behavior. The diffusion coefficient "*D*" strongly relies on concentration for many polymer/penetrant systems. For example, organic vapors or solvents require an appropriate movement of a polymer chain segment to form an optimum-sized 'hole.' However, the diffusion kinetics can still be Fickian even above the glass transition temperature ($T_g$) of a polymer, and below $T_g$ will give rise to time-resolved non-Fickian effects because polymer chain segments need a restricted rearrangement time to accommodate the diffusing penetrant molecules.

As per the classification reported by Alfrey et al. (1966), the comparative rates of relaxation in polymer segments and mobility of permeant are two important bases on which diffusion in polymers can be classified. In the case where the relaxation of the polymer segment is faster than the permeant mobility, the diffusion is termed Fickian (or CASE I diffusion). It quantifies the absorbed permeant/unit area at a time '$t$' and can be represented by the relation '$M_t = Kt^n$' where '$K$' and '$n$' are constants, and for any system that shows Fickian diffusion, $n$=1/2.

Alternatively, if the relaxation of the polymer segment is slower than the permeant, it is referred to as CASE II diffusion. In such diffusions, a sharp boundary comprised of an unswollen glassy core between the inner region and the outer swollen layer occurs, which moves towards the glassy core with constant velocity. In CASE II diffusion, n=1. This pattern typically arises when the permeant causes significant swelling in polymers, a behavior not observed with simple gases or liquids. Alfrey et al. (1966) identified an intermediate diffusion category, referred to as "anomalous" diffusion, characterized by $1/2 < n < 1$. The observed water absorption behavior aligns with Fickian diffusion principles (Sergi et al., 2019).

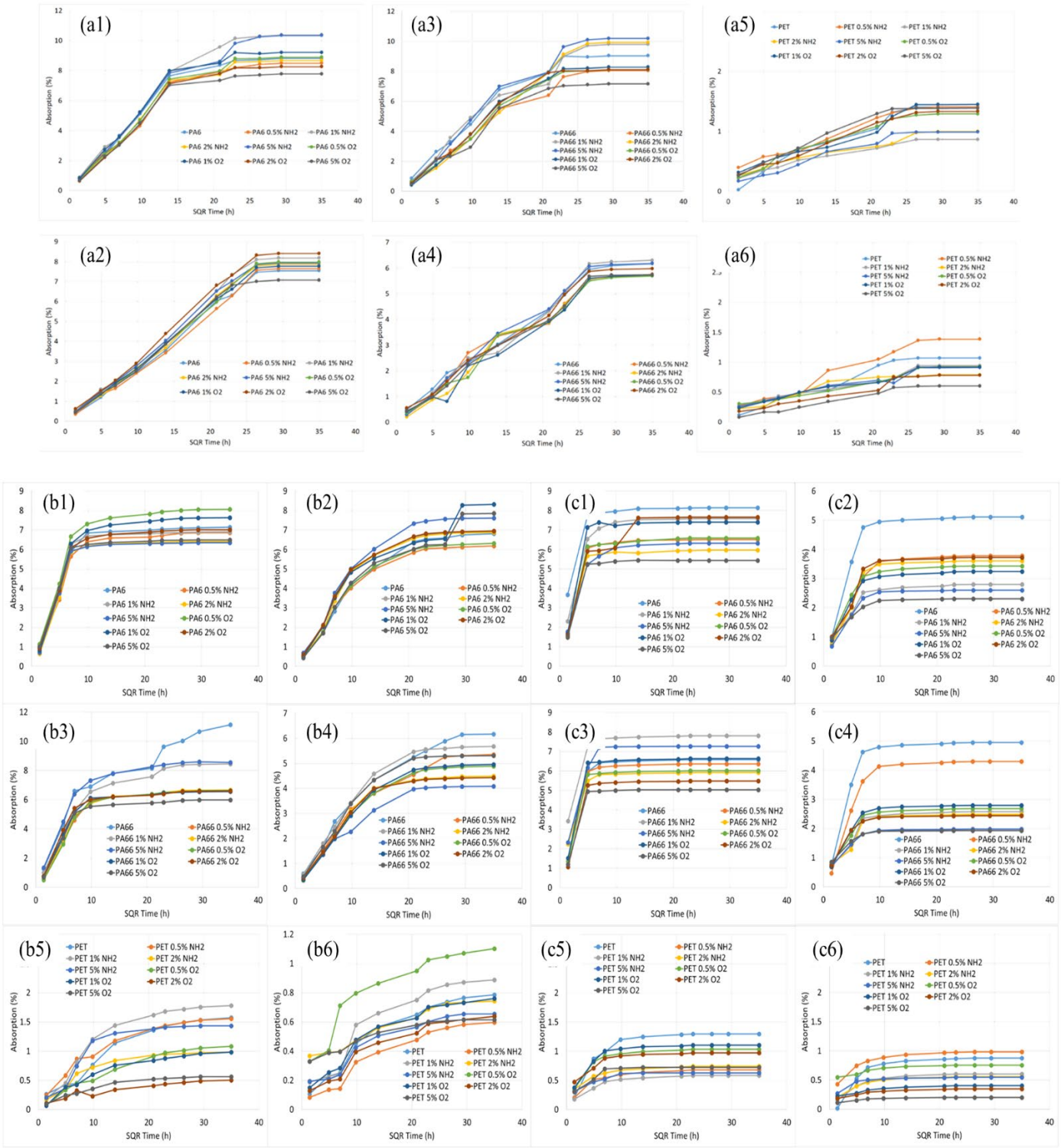


**Fig. 6. (a)** Water absorption measured in terms of (%) weight gain against the square root of time measured for (left) 1mm and (right) 2mm thick (a1, a2) PA6, (a3, a4) PA66 and (a5, a6) PET samples loaded with 0.5, 1, 2 and 5% $NH_2$ and $O_2$ functionalized graphene at 23 °C. (b) Water absorption measured in terms of (%) weight gain against the square root of time measured for (left) 1mm and (right) 2mm thick (b1, b2) PA6, (b3, b4) PA66, and (b5, b6) PET samples loaded with 0.5, 1, 2 and 5% $NH_2$ and $O_2$ functionalized graphene at 40 °C. (c) Water absorption measured in terms of (%) weight gain against the square root of time measured for (left) 1mm and (right) 2mm thick (c1, c2) PA6, (c3, c4) PA66, and (c5, c6) PET samples loaded with 0.5, 1, 2 and 5% $NH_2$ and $O_2$ functionalized graphene at 70 °C. (Each experimental point is a mean of three equal experiments ($n$=3). The maximum standard error was 0.65%).

Figure 6c shows the water uptake results at 70 °C. The saturation time was reduced to circa 1/3 of the room temperature samples in all cases at 70 °C. All the samples showed a sharp initial absorption followed by a steady saturation trend and quickly achieved an effective equilibrium. For PA6 samples, pristine polymers experienced the highest absorption in both thickness variants, while PA6 5% $O_2$ samples exhibited the lowest absorption values. Also, PA66 showed the same trend for the lowest absorption, while 1% $NH_2$ and pristine samples showed the highest absorption for 1 and 2-mm-thick samples, respectively.

In the case of PET, pristine and 0.5% $NH_2$ samples showed the highest absorption, while 1% $NH_2$ and 5% $O_2$ samples showed the lowest absorption for 1 and 2-mm-thick samples, respectively. Interestingly, in most cases for all three polymer matrices, the 5% $O_2$ sample exhibited the lowest absorption. Table 3 summarizes the history of the moisture uptake of all the samples (with 1 and 2mm thickness variants) with various loadings of $O_2$ and $NH_2$ functionalized graphene as a function of the square root of time (hours).

**Table 3:** Lowest and highest moisture uptake (% weight gain) values as a function of the square root of time for PA6, PA66, and PET samples loaded with 0.5, 1, 2, and 5% $NH_2$ and $O_2$ functionalized graphene at 23, 40, and 70 °C.

| T (°C) | Water absorption (%) | Samples with (%) $O_2$ and $NH_2$ loadings | | | | | |
|---|---|---|---|---|---|---|---|
| | | PA6 | | PA66 | | PET | |
| | | 1mm | 2mm | 1mm | 2mm | 1mm | 2mm |
| 23 | Lowest | 5 % $O_2$ | 5 % $O_2$ | 5 % $O_2$ | 0.5 % $O_2$ | 1 % $NH_2$ | 5 % $O_2$ |
| | Highest | 1 % $NH_2$ | 2 % $O_2$ | 5 % $NH_2$ | 1 % $NH_2$ | 1 % $O_2$ | 0.5% $NH_2$ |
| 40 | Lowest | 5 % $NH_2$ | 0.5%$NH_2$ | 5 % $O_2$ | 5 % $NH_2$ | 2 % $O_2$ | 0.5%$NH_2$ |
| | Highest | 0.5 % $O_2$ | 1 % $O_2$ | Pristine | Pristine | 1 % $NH_2$ | 0.5 % $O_2$ |
| 70 | Lowest | 5 % $O_2$ | 5 % $O_2$ | 5 % $O_2$ | 5 % $O_2$ | 1 % $NH_2$ | 5 % $O_2$ |
| | Highest | Pristine | Pristine | 1 % $NH_2$ | Pristine | Pristine | 0.5%$NH_2$ |

Diffusion Coefficient based on the fundamentals in the mechanistic study of the water absorption in polymeric systems, the water absorption behavior of a material correlates to the immersion environment in terms of temperature at a constant humidity (65% RH). Additionally, the slope of the initial stage in the water absorption curve indicates that water absorption increases with higher temperatures. This increase in temperature accelerates the water absorption rate of a composite. Also, the saturation time for water absorption reduces with increasing temperature. Water absorption occurs due to the irregular motion of numerous water molecules, and elevated temperatures actually accelerate that motion and thus reach saturation in a short time (Wang et al. 2020). Figures 12-14 also show similar behavior, and the samples tested at room temperature took significantly more time to reach saturation than those tested at 40 °C or 70 °C. The time to saturation at 40 °C and 70 °C was reduced to more than half and, in some cases, 1/3 compared to the saturation time at room temperature. Another possible explanation is that the water solubility in polymeric systems and their composite is likely to increase with temperature because the free volume of polymers increases with increasing temperature, ultimately allowing more water uptake in that additional volume. This trend has been reported by many researchers (Papanicolaou and Pappa 1992, Xiang and Jones 1997, Karbhari et al. 2009). This phenomenon occurs due to an increase in thermal energy, which consequently increases the mobility of the water molecules and the segmental motion of the polymer chains. As a result, it allows more water to penetrate the high-density regions, as Sahlin and Peppas (1991) reported. Another suggestion, as reported by Vanlandingham et al. (1999), is that elevated temperatures cause cracking, chalking, and flaking of polymers, which ultimately allows more water to penetrate,

which is not investigated in the current study. Therefore, it can be deduced that the diffusion rate of water molecules can be significantly accelerated at increasing temperatures, ultimately achieving the effective equilibrium rapidly.

This study uses the Fickian model to determine Fickian diffusion and calculate the equilibrium level, necessitating the extraction of Fickian parameters from the curve. Several investigations have observed similar phenomena. Gautier et al. and Hodzic et al. identified the formation of matrix microcracks due to interfacial debonding, differential swelling, and osmotic cracking in a hydrothermal environment (Hodzic et al., 2004). Huang and Sun (2005) also found that prolonged immersion time accelerates water absorption due to capillary action and the absorption of hydrophilic groups. Ellyin and Maser (2004) reported that increased water temperature enhances temperature-dependent damage at the interface between the filler and polymer matrix. Consequently, matrix swelling, interphase debonding, and hydrolysis of epoxy are crucial factors influencing the properties of polymers and their composites.

Polymers such as PA6 and PA66 (used in this study) are semicrystalline thermoplastic polymers and exhibit excellent properties such as low density, high mechanical strength, and abrasion resistance (Gupta et al. 2006). However, they tend to absorb surrounding moisture because of their polar amide groups in their structure. Ultimately, it leads to the instability of the material (Bouhfid et al. 2016), which limits its applications. Diffusion of water from external resources leads to the plasticization and the hydrolysis of the molecular backbone of the polymers, ultimately deteriorating their properties (Le Gac et al. 2017). Moisture absorption can deteriorate the properties (particularly, the mechanical properties) of the polymer composites following three

distinguished mechanisms. Firstly, water molecules diffuse within the microlactes between the polymer chains. The second includes the capillary transport in gaps and faults at the interfaces between the filler and matrix, while the third is due to the swelling effect that ultimately initiates microcracks in the matrix (Santos et al. 2019). However, adding fillers such as graphene particles yielded composite materials with controllable absorption and improved properties (Botan et al. 2018).

Karbhari and Xian (2009), along with earlier work by Tsotsis and Weitsman (1994), proposed a straightforward model for calculating quasi-equilibrium moisture uptake by drawing tangents to the weight gain versus the square root of time curve at both the initial and leveling-off stages. The intersection point represents the maximum moisture level corresponding to the first diffusion stage. Fickian and long-term behaviors can be distinguished by drawing a tangent to the moisture weight gain curve in the long-term diffusion region and fitting it to the Fickian diffusion curve, as shown in Figure S2. The tangent gradient ($G_{LT}$) is determined to achieve the best fit to the Fickian diffusion curve, and the quasi-equilibrium moisture content ($M_t^{new}$) is calculated using Eq. 3. All the first absorption curves and calculated equilibrium moisture values have been summarized by employing the method above. Further, the diffusion rates for absorption were calculated as described by Korkees (2012) and are presented in Section S1 of the supplementary material.

$$M_t^{new} = M_t^{old} - GLT\sqrt{t} \qquad \text{Eq. 3}$$

The water absorption behavior of a material in polymeric systems is closely related to the immersion environment, particularly the temperature, at a constant humidity of 65% RH. The initial slope of the water absorption curve suggests that as

temperature increases, water absorption also increases. This acceleration in absorption rate is primarily due to the enhanced molecular motion at higher temperatures, which leads to faster saturation. Figure 6 illustrates this trend, showing that samples tested at room temperature took significantly longer to reach saturation compared to those tested at 40 °C or 70 °C. At 40 °C and 70 °C, the saturation time was reduced by more than half, and in some cases, to one-third of the time required at room temperature.

An additional factor contributing to this behavior is the increased solubility of water in polymeric systems at elevated temperatures. As temperature rises, the free volume of polymers expands, allowing for greater water uptake in that additional volume. This trend occurs due to the increase in thermal energy, which enhances the mobility of both water molecules and polymer chains, facilitating water penetration into the high-density regions (Sahlin and Peppas, 1991). Another possible explanation is that elevated temperatures can cause damage to the polymer, such as cracking, chalking, and flaking, which may further facilitate water penetration. However, this phenomenon was not explored in the current study. Overall, it can be deduced that increasing temperature significantly accelerates the diffusion rate of water molecules, resulting in rapid attainment of effective equilibrium (Vanlandingham et al., 1999).

Figure 6 and S2 also demonstrate the influence of sample thickness on absorption capacity. For instance, in the case of PA6 at 23 °C, the 1 mm thick samples reached saturation after approximately 225 hours, while the 2 mm thick samples took around 625 hours, nearly three times longer. This trend was consistent for all graphene variants of the PA6 samples. At 40 °C, the difference in saturation time between the two thicknesses was even more pronounced, with the 2 mm samples reaching saturation after 220 hours,

compared to just 36 hours for the 1 mm samples. However, at 70 °C, the difference in saturation time between the two thicknesses diminished significantly, suggesting that temperature plays a more prominent role in reducing saturation time than thickness.

In terms of equilibrium moisture content, the sample thickness also affected the maximum absorption values. At 23 °C, the 1 mm samples absorbed nearly 20% more moisture than the 2 mm samples. This difference became less significant at 40 °C, but at 70 °C, the 1 mm samples absorbed almost double the moisture compared to the 2 mm samples. For the PA66 samples, the 1 mm samples reached saturation after 400 hours, while the 2 mm samples took about 625 hours. Although the difference in saturation time at 23 °C was smaller for PA66 than for PA6, the absorption values for the 2 mm samples were only about 60% of the values for the 1 mm samples. At 40 °C, the 1 mm samples reached saturation after approximately 100 hours, while the 2 mm samples took about 225 hours, and the absorption values for the 1 mm samples were 20 to 40% higher than for the 2 mm samples. At 70 °C, the saturation times for the two thickness variants were similar, but the absorption values for the 1 mm samples were significantly higher.

For the PET samples, the saturation times and absorption values were nearly identical for both thickness variants at 23 °C. A slight difference in absorption values was observed at 40 °C, with the 1 mm samples showing higher absorption than the 2 mm samples. A similar trend was seen at 70 °C, though the difference in absorption values between the two thickness variants was negligible. This consistency in saturation values, despite the thickness differences, can be attributed to the higher temperatures, which enhance the mobility of water molecules and the segmental motion of polymer chains,

allowing more water to penetrate the high-density regions. In Fig. 7, the diffusion coefficients for the two different thicknesses employed in this study are presented.

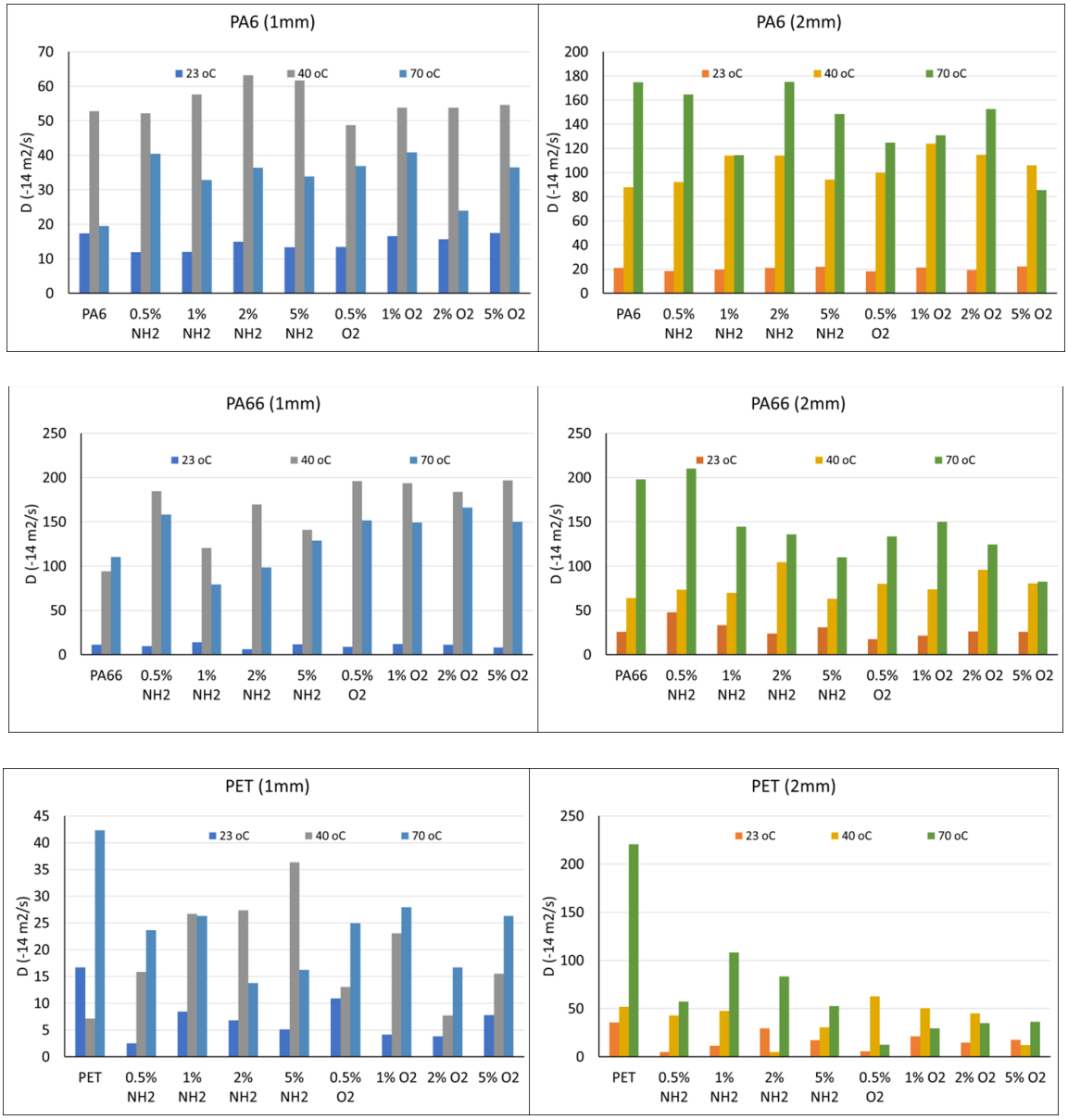


**Fig. 7.** Diffusion coefficients of 1 and 2-mm-thick PA6, PA66, and PET samples for all functionalized loadings at 23, 40, and 70 ºC. (Each experimental point is a mean of three equal experiments ($n$=3). The maximum standard error was 1.96%).

The diffusion coefficient is a key parameter for assessing water penetration and absorption rates over time. Various factors, including the diffusivities of the components,

the moisture concentration in the environment, and the temperature, influence it. Typically, diffusion is a temperature-dependent process, meaning the diffusion coefficient is highly sensitive to the temperature of the surrounding moisture. Temperature dependency of the diffusion coefficient can also be expressed using the Arrhenius equation, which gives a linear relation when plotting *ln(D)* versus *1/T.* Korkees (2012) reported that diffusion coefficient values increase when the temperature increases, which also increases short-term diffusion.

In this context, Karbhari et al. reported that the diffusion coefficient is directly proportional to the immersion time ascribed to the new pathways for the diffusion owing to micro-cracks causing swelling of polymeric composites (Karbhari and Xian 2009). In another report by Bao and Yee (2002), a 10 times increase in diffusion coefficient was observed at a temperature increase of 55 °C. This phenomenon has been attributed to the rapid molecular mobility at an elevated temperature that ultimately provides an enhanced volume to the molecules because of their thermally activated vibrational motion. In another study, Broughton et al. investigated the fiber-reinforced polymeric composites for which a five times increase in the diffusivity was observed at a temperature range between 25 and 60 °C (Broughton and Lodeiro 2000).

Figures 6a, 6b, and 6c, as well as Fig. S2, exhibit a typical Fickian diffusion behavior in the initial stage, followed by a slow increase in the absorption content leading toward the saturation point. The results of the current study are consistent with several previous studies showing two points of diffusion (Choi et al. 2001). Hence, the linear relationship between absorption (% weight gain) and the square root of time indicates the two stages of water uptake. The initial diffusion-controlled water absorption has been

widely reported (Cândido et al. 2008). The gradual increase in moisture content during the second stage of water uptake can be attributed to the development of strong hydrogen bonds between water and polar groups within the polymers, facilitating increased water ingress. Another reason could be the polymer relaxation that can cause more water to diffuse because both the polymer relaxation and moisture diffusion are temperature-sensitive processes.

Furthermore, water is believed to be a good plasticizer of a polymeric material, and it is believed to induce structural relaxation in all the hydrothermally aged samples, which ultimately enables more pockets of free volume to occupy the water molecules. In this regard, several researchers attributed the two-stage water uptake phenomenon to the relaxation of the polymer chain (Berens 1977, Berens and Hopfenberg 1978). Several reports have also confirmed that water-induced chemical degradation could be a reason for the two-stage water diffusion. Hence, the temperature increase can potentially change a polymer matrix's physical and chemical characteristics due to several processes and hydrolysis (Ellyin and Maser 2004). It is noteworthy that the diffusion process is much faster than structural relaxation. Therefore, the first stage is attributed to diffusion control, while the second stage can be ascribed to relaxation control (Bao et al. 2001).

### *3.5. Effect of functionalized graphene nanoparticles on water diffusion behavior*

It is evident from the results of the current study that the inclusion of GNPs has significantly enhanced the barrier performance to moisture of the polymers. The mechanism behind the performance enhancement via the inclusion of functionalized graphene can be explained for several reasons based on the results of the current study

and previously reported findings of the researchers (Korkees, 2012). Firstly, as can be seen in the SEM images of the sample, large flakes are visible at higher filler concentrations, and these large flakes force the water molecules to follow a longer tortuous path in the polymer matrix. Hence, it promotes much longer diffusion paths because these partially aligned large flakes in the film are perpendicular to the water vapor flow. However, the longer tortuous paths owing to graphene filler are not the only reason for improved barrier properties. For instance, oxygen functional groups such as hydroxyl, epoxide, carbonyl, and carboxyl on the basal planes and edges significantly improve the interfacial bonding between graphene and the polymer matrix. A whole class of polar interactions enables new strong interfaces, such as the Coulombic and polar interactions and the hydrogen bonding, in addition to the covalent bonding. Hence, oxygen functionalities enable enhanced interaction with the polymer matrices, and ultimately, a uniform dispersion can be achieved. Moreover, graphene nanofillers tend to self-align at higher concentrations, typically above 2 wt.%, which is reportedly at an optimum level of 5 wt.% [36], and has been deduced during the current study too. The lower concentration yields good dispersion of fillers in the polymer matrix.

However, filler concentration in the polymer matrix is a critical factor. Filler concentration should not exceed a certain limit and has to be optimized, as in the current study case, because the permeability can be significantly reduced at very high concentrations. As the concentration increases, the viscosity rises to a point where absorption starts to decrease and eventually levels off. This rise in viscosity is known as the rheological percolation threshold (Sun et al., 2009), which corresponds to a concentration where a sharp increase in viscosity occurs due to strong physical

interactions between the fillers, restricting the mobility of the polymer chains (Willenbacher and Georgieva, 2013). When the viscosity surpasses the percolation threshold, it greatly impairs the workability of the matrix, and its porosity increases due to air entrapment. In this context, Damari et al. reported 7% filler concentration, and during permeability tests, they observed sharp degradation in the barrier properties of the nanocomposite. Some of the results of this work also indicate the uniform distribution of filler into the polymer matrices. However, due to the large aspect ratio of the graphene fillers, the diffusion of the water can be significantly reduced.

## 4. Conclusion

This study demonstrates the potential of using $O_2$- and $NH_2$-functionalised graphene nanofillers to enhance the barrier properties of recycled PA6, PA66, and PET matrices to moisture. The composite films with different loading concentrations and thickness variants were prepared and tested for water vapor transmission rate and absorption. The SEM results suggest different degrees of interfacial interactions between the fillers and the polymer matrices, and the amine group showed superior bonding compared to $O_2$ functionalization. The choice between $O_2$ and $NH_2$ functionalization of graphene significantly impacts the interface interactions in graphene/polymer composites. $NH_2$ functionalization generally leads to stronger covalent bonding and better mechanical properties, while $O_2$ functionalization may enhance dispersion but with less impact on interfacial strength. The addition of graphene fillers improves the barrier properties of the polymer matrices, but the degree of improvement varies with loading concentration and

functionalization type. Oxygen-containing groups (e.g., hydroxyl, carboxyl) on the surface of graphene enhanced the hydrophilicity of graphene, which improved its dispersion in polar polymer matrices like Nylon 6 and Nylon 66 through strong hydrogen bonding interactions with the amide groups. $NH_2$ functionalization increases the reactivity of graphene and can enhance its compatibility with Nylon and PET.

The mass loss for the 0.5 mm thickness is significantly lower than that for the 0.09 mm thickness. Additionally, the mass loss values are influenced by the type of functionalization used. In this regard, composites with $O_2$-functionalized graphene exhibit less mass loss compared to those with $NH_2$-functionalized polymeric systems. Graphene fillers over 2 wt.% exhibit a significant orientation of graphene sheets, as they tend to self-adjust their basal plane perpendicular to the film thickness, resulting in partial alignment of the graphene layers.

The slope of the initial phase in the water absorption curve shows that water absorption rises with higher temperatures. This temperature increase speeds up the water absorption rate of the composite. Additionally, the time taken to reach saturation for water absorption decreases as the temperature increases. Overall, this study provides useful insights into the potential of using graphene fillers to enhance the properties of recycled polymer matrices, which could have important implications for reducing the environmental impact of plastics.

**Funding information**

No funding was received.

**References**


Agbangba, C.E., et al., On the use of post-hoc tests in environmental and biological sciences: A critical review. Heliyon, 2024. 10(3): p. e25131.

Alfrey Jr, T., E. Gurnee, and W. Lloyd. Diffusion in glassy polymers. in Journal of Polymer Science Part C: Polymer Symposia. 1966. Wiley Online Library.

Ansari, S., et al., Oriented arrays of graphene in a polymer matrix by in situ reduction of graphite oxide nanosheets. Small, 2010. 6(2): p. 205-209.

Bao, L.-R. and A.F. Yee, Moisture diffusion and hygrothermal aging in bismaleimide matrix carbon fiber composites—part I: uni-weave composites. Composites Science and Technology, 2002. 62(16): p. 2099-2110.

Bao, L.-R., A.F. Yee, and C.Y.-C. Lee, Moisture absorption and hygrothermal aging in a bismaleimide resin. polymer, 2001. 42(17): p. 7327-7333.

Bell, L. and T. Labuza, Moisture sorption: practical aspects of isotherm measurement and use. American association of cereal chemists. Inc., St. Paul, 2000: p. 33-36.

Berens, A., Diffusion and relaxation in glassy polymer powders: 1. Fickian diffusion of vinyl chloride in poly (vinyl choride). Polymer, 1977. 18(7): p. 697-704.

Berens, A.R. and H.B. Hopfenberg, Diffusion and relaxation in glassy polymer powders: 2. Separation of diffusion and relaxation parameters. Polymer, 1978. 19(5): p. 489-496.

Botan, R., et al., Correlation between water absorption and mechanical properties of polyamide 6 filled with layered double hydroxides (LDH). Materials research express, 2018. 5(6): p. 065004.

Bouhfid, R., F. Arrakhiz, and A. Qaiss, Effect of graphene nanosheets on the mechanical, electrical, and rheological properties of polyamide 6/acrylonitrile–butadiene–styrene blends. Polymer Composites, 2016. 37(4): p. 998-1006.

Broughton, W. and M. Lodeiro, Techniques for monitoring water absorption in fibre-reinforced polymer composites. 2000.

Cândido, G., et al., Hygrothermal effects on quasi-isotropic carbon epoxy laminates with machined and molded edges. Composites Part B: Engineering, 2008. 39(3): p. 490-496.

Cho, J., et al., Improving dispersion and barrier properties of polyketone/graphene nanoplatelet composites via non-covalent functionalization using aminopyrene. ACS applied materials & interfaces, 2017. 9(33): p. 27984-27994.

Choi, H., et al., Hygroscopic aspects of epoxy/carbon fiber composite laminates in aircraft environments. Composites Part A: applied science and manufacturing, 2001. 32(5): p. 709-720.

Damari, S.P., et al., Graphene-induced enhancement of water vapor barrier in polymer nanocomposites. Composites Part B: Engineering, 2018. 134: p. 218-224.

Duncan, B. and W. Broughton, Absorption and diffusion of moisture in polymeric materials. 2007.

Ellyin, F. and R. Maser, Environmental effects on the mechanical properties of glass-fiber epoxy composite tubular specimens. Composites Science and Technology, 2004. 64(12): p. 1863-1874.

Feron, V., et al., Polyethylene terephthalate bottles (PRBs): a health and safety assessment. Food Additives & Contaminants, 1994. 11(5): p. 571-594.

Gojny, F.H., et al., Influence of different carbon nanotubes on the mechanical properties of epoxy matrix composites–a comparative study. Composites science and technology, 2005. 65(15-16): p. 2300-2313.

Guan, Y., Barrier Properties of Polymer Nanocomposites with Graphene Oxide and Its Derivatives: Mechanism and Applications in Anticorrosive Coatings. 2017, The University of Southern Mississippi.

Gupta, B., M.-F. Lacrampe, and P. Krawczak, Polyamide-6/clay nanocomposites: a critical review. Polymers and Polymer Composites, 2006. 14(1): p. 13-38.

Hodzic, A., et al., The effects of water aging on the interphase region and interlaminar fracture toughness in polymer–glass composites. Composites science and technology, 2004. 64(13-14): p. 2185-2195.

Huang, C., et al., Cryogenic properties of SiO2/epoxy nanocomposites. Cryogenics, 2005. 45(6): p. 450-454.

Huang, H.-D., et al., Ultra-low gas permeability and efficient reinforcement of cellulose nanocomposite films by well-aligned graphene oxide nanosheets. Journal of Materials Chemistry A, 2014. 2(38): p. 15853-15863.

Huang, J.C., Carbon black filled conducting polymers and polymer blends. Advances in Polymer Technology: Journal of the Polymer Processing Institute, 2002. 21(4): p. 299-313.

Hwang, S.-T. and K. Kammermeyer, Effect of thickness on permeability, in permeability of plastic films and coatings. 1974, Springer. p. 197-205.

Karbhari, V.M. and G. Xian, Hygrothermal effects on high VF pultruded unidirectional carbon/epoxy composites: Moisture uptake. Composites Part B: Engineering, 2009. 40(1): p. 41-49.

Keledi, G., J. Hari, and B. Pukanszky, Polymer nanocomposites: structure, interaction, and functionality. Nanoscale, 2012. 4(6): p. 1919-1938.

Keller, P.E. and R.T. Kouzes, Water vapor permeation in plastics. 2017, Pacific Northwest National Lab.(PNNL), Richland, WA (United States).

Kim, H. and C.W. Macosko, Morphology and properties of polyester/exfoliated graphite nanocomposites. 2008.

Korkees, F., et al., Functionalised graphene effect on the mechanical and thermal properties of recycled PA6/PA6,6 blends. Journal of Composite Materials, 2021. 55(16): p. 2211-2224.

Korkees, F., et al., Functionalised graphene effect on the mechanical and thermal properties of recycled PA6/PA6, 6 blends. Journal of Composite Materials, 2021: p. 0021998320987897.

Korkees, F., Modelling of water absorption into carbon fibre/epoxy composites. 2012, Swansea University.

Le Gac, P.-Y., et al., Yield stress changes induced by water in polyamide 6: characterization and modeling. Polymer Degradation and Stability, 2017. 137: p. 272-280.

Li, J. and J.-K. Kim, Percolation threshold of conducting polymer composites containing 3D randomly distributed graphite nanoplatelets. Composites science and technology, 2007. 67(10): p. 2114-2120.

Li, J., E. Gunister, and I. Barsoum, Effect of graphene oxide as a filler material on the mechanical properties of LLDPE nanocomposites. Journal of Composite Materials, 2019. 53(19): p. 2761-2773.

Liu, W., et al., Influence of processing on morphology, electrical conductivity and flexural properties of exfoliated graphite nanoplatelets-polyamide nanocomposites. Carbon letters, 2010. 11(4): p. 279-284.

Lizundia, E., et al., Free-volume effects on the thermomechanical performance of epoxy–SiO2 nanocomposites. Journal of Applied Polymer Science, 2017. 134(34): p. 45216.

Ma, P.-C., et al., dispersion and functionalization of carbon nanotubes for polymer-based nanocomposites: A review. Composites Part A: Applied Science and Manufacturing, 2010. 41(10): p. 1345-1367.

Ma, T., et al., Tailoring the thermal and electrical transport properties of graphene films by grain size engineering. Nature communications, 2017. 8(1): p. 1-9.

Mahmoud, A., et al., Novel sulfonated poly (vinyl alcohol)/Carboxy methyl Cellulose/ Acrylamide - based hybrid polyelectrolyte membranes, Scientific Reports, 2022.12: 22017.

Mahmoud, A., et al, Synthesis and characterization of nylon 6,6-polyvinyl alcohol-based polyelectrolytic membrane, Arabian Journal for Science and Engineering, 2023. 48: p. 8941-8956.

Méndez, R., et al., Barrier, mechanical and conductive properties of polycaprolactam nanocomposites containing carbon-based particles: Effect of the kind of particle. Polymer, 2017. 130: p. 10-16.

Mkhoyan, K.A., et al., Atomic and electronic structure of graphene-oxide. Nano letters, 2009. 9(3): p. 1058-1063.

Moghadam, A.D., et al., Mechanical and tribological properties of self-lubricating metal matrix nanocomposites reinforced by carbon nanotubes (CNTs) and graphene–a review. Composites Part B: Engineering, 2015. 77: p. 402-420.

Naskar, A.K., J.K. Keum, and R.G. Boeman, Polymer matrix nanocomposites for automotive structural components. Nature nanotechnology, 2016. 11(12): p. 1026-1030.

Okada, A., et al., Synthesis and properties of nylon-6/clay hybrids. Polymer based molecular composites, 1990. 171: p. 45-50.

Papanicolaou, G. and A. Pappa, Water sorption and temperature effects on the dynamic mechanical behaviour of epoxy-matrix particulates. Journal of materials science, 1992. 27(14): p. 3889-3896.

Rajasekar, R., et al., Electrostatically assembled layer-by-layer composites containing graphene oxide for enhanced hydrogen gas barrier application. Composites science and technology, 2013. 89: p. 167-174.

Riaz, U. and S.M. Ashraf, Characterization of polymer blends with FTIR spectroscopy. Characterization of polymer blends, 2014: p. 625-678.

Sahlin, J.J. and N.A. Peppas, Penetrant transport in epoxy resins. Industrial & engineering chemistry research, 1991. 30(1): p. 211-217.

Salame, M. and S. Steingiser, Barrier polymers. 1977.

Sangaj, N.S. and V. Malshe, Permeability of polymers in protective organic coatings. Progress in Organic coatings, 2004. 50(1): p. 28-39.

Sangroniz, A., et al., Packaging materials with desired mechanical and barrier properties and full chemical recyclability. Nature communications, 2019. 10(1): p. 1-7.

Santos, W.R.G.d., M.K.T.d. Brito, and A.G.B.d. Lima, Study of the moisture absorption in polymer composites reinforced with vegetal fiber using Langmuir's model. Materials Research, 2019. 22.

Sergi, C., et al., Durability of basalt/hemp hybrid thermoplastic composites. Polymers, 2019. 11(4): p. 603.

Shen, C.-H. and G.S. Springer, Moisture absorption and desorption of composite materials. Journal of composite materials, 1976. 10(1): p. 2-20.

Shogren, R., Water vapor permeability of biodegradable polymers Journal of environmental polymer degradation, 1997. 5: p. 91-95.

Sun, L., et al., effect of nanoplatelets on the rheological behavior of epoxy monomers. Macromolecular Materials and Engineering, 2009. 294(2): p. 103-113.

Sun, X., et al., Recent progress in graphene/polymer nanocomposites. Advanced Materials, 2021. 33(6): p. 2001105.

Tan, B. and NL. Thomas, A review of the water barrier properties of polymer/clay and polymer/graphene nanocomposites. Journal of Membrane Science, 2016. 514: p. 595-612.

Tang, X. and E.Y.-X. Chen, Toward infinitely recyclable plastics derived from renewable cyclic esters. Chem, 2019. 5(2): p. 284-312.

Terrones, M., et al., Interphases in graphene polymer-based nanocomposites: Achievements and challenges. Advanced Materials, 2011. 23(44): p. 5302-5310.

Tseng, I.-H., et al., Transparent polyimide/graphene oxide nanocomposite with improved moisture barrier property. Materials Chemistry and Physics, 2012. 136(1): p. 247-253.

Tsotsis, T. and Y. Weitsman, A simple graphical method for determining diffusion parameters for two-stage sorption in composites. Journal of materials science letters, 1994. 13(22): p. 1635-1636.

Vanlandingham, M., R. Eduljee, and J. Gillespie Jr, Moisture diffusion in epoxy systems. Journal of applied polymer science, 1999. 71(5): p. 787-798.

Verdejo, R., et al., graphene filled polymer nanocomposites. Journal of Materials Chemistry, 2011. 21(10): p. 3301-3310.

Wang, W., et al., Water absorption and hygrothermal aging behavior of wood-polypropylene composites. Polymers, 2020. 12(4): p. 782.

Willenbacher, N. and K. Georgieva, Rheology of disperse systems. Product design and engineering: Formulation of gels and pastes, 2013: p. 7-49.

Wu, Z., et al., Synergistic effect of aligned graphene nanosheets in graphene foam for high-performance thermally conductive composites. Advanced Materials, 2019. 31(19): p. 1900199.

Xiang, Z. and F. Jones, Thermal-spike-enhanced moisture absorption by polymer-matrix carbon-fibre composites. Composites Science and Technology, 1997. 57(4): p. 451-461.

Xu, B.F., et al., Mechanical properties, morphology and thermal conductivity of polyamide composites filled with graphene nanoplatelets, Al2O3 and graphite. Materials Research Innovations, 2015. 19(sup1): p. S1-388-S1-391.

Yang, Y.-K., et al., Non-covalently modified graphene sheets by imidazolium ionic liquids for multifunctional polymer nanocomposites. Journal of Materials Chemistry, 2012. 22(12): p. 5666-5675.

Yousefi, N., et al., Highly aligned, ultralarge-size reduced graphene oxide/polyurethane nanocomposites: mechanical properties and moisture permeability. Composites Part A: Applied Science and Manufacturing, 2013. 49: p. 42-50.

Yousefi, N., et al., Self-alignment and high electrical conductivity of ultralarge graphene oxide–polyurethane nanocomposites. Journal of Materials Chemistry, 2012. 22(25): p. 12709-12717.

Yu, X., et al., Graphene-based smart materials. Nature Reviews Materials, 2017.

Zahid, M., et al., Graphene morphology effect on the gas barrier, mechanical and thermal properties of thermoplastic polyurethane. Composites Science and Technology, 2020. 200: p. 108461.

Zeinedini, A., M.M. Shokrieh, and A. Ebrahimi, The effect of agglomeration on the fracture toughness of CNTs-reinforced nanocomposites. Theoretical and Applied Fracture Mechanics, 2018. 94: p. 84-94.